CHALMERS
UNIVERSITY OF TECHNOLOGY

Milliarcsecond Localization of the Repeating FRB 20201124A

The Astrophysical Journal Letters, 927:L3 (12pp), 2022 March 1 https://doi.org/10.3847/2041-8213/ac540f

Milliarcsecond Localization of the Repeating FRB 20201124A

K. Nimmo[1,2], D. M. Hewitt[2], J. W. T. Hessels[1,2], F. Kirsten[1,3], B. Marcote[4], U. Bach[5], R. Blaauw[1], M. Burgay[6], A. Corongiu[6], R. Feiler[7], M. P. Gawroński[7], M. Giroletti[8], R. Karuppusamy[5], A. Keimpema[4], M. A. Kharinov[9], M. Lindqvist[3], G. Maccaferri[8], A. Melnikov[9], A. Mikhailov[9], O. S. Ould-Boukattine[2], Z. Paragi[4], M. Pilia[6], A. Possenti[6], M. P. Snelders[2], G. Surcis[6], M. Trudu[6], T. Venturi[8], W. Vlemmings[3], N. Wang[10], J. Yang[3], and J. Yuan[10]

[1] ASTRON, Netherlands Institute for Radio Astronomy, Oude Hoogeveensedijk 4, 7991 PD Dwingeloo, The Netherlands; k.nimmo@uva.nl
[2] Anton Pannekoek Institute for Astronomy, University of Amsterdam, Science Park 904, 1098 XH, Amsterdam, The Netherlands
[3] Department of Space, Earth and Environment, Chalmers University of Technology, Onsala Space Observatory, SE-439 92 Onsala, Sweden
[4] Joint Institute for VLBI ERIC (JIVE), Oude Hoogeveensedijk 4, 7991PD Dwingeloo, The Netherlands
[5] Max-Planck-Institut für Radioastronomie, Auf dem Hügel 69, D-53121 Bonn, Germany
[6] Istituto Nazionale di Astrofisica, Osservatorio Astronomico di Cagliari, Via della Scienza 5, I-09047, Selargius, Italy
[7] Institute of Astronomy, Faculty of Physics, Astronomy and Informatics, Nicolaus Copernicus University, Grudziadzka 5, 87-100 Toruń, Poland
[8] Istituto Nazionale di Astrofisica, Istituto di Radioastronomia, Via Gobetti 101, I-40129, Bologna, Italy
[9] Institute of Applied Astronomy, Russian Academy of Sciences, Kutuzova Embankment 10, St. Petersburg, 191187, Russia
[10] Xinjiang Astronomical Observatory, 150 Science 1-Street, Urumqi, Xinjiang 830011, People's Republic of China
Received 2021 November 2; revised 2022 February 4; accepted 2022 February 11; published 2022 March 1

Abstract

Very long baseline interferometric (VLBI) localizations of repeating fast radio bursts (FRBs) have demonstrated a diversity of local environments: from nearby star-forming regions to globular clusters. Here we report the VLBI localization of FRB 20201124A using an ad hoc array of dishes that also participate in the European VLBI Network (EVN). In our campaign, we detected 18 bursts from FRB 20201124A at two separate epochs. By combining the visibilities from both epochs, we were able to localize FRB 20201124A with a 1σ uncertainty of 2.7 mas. We use the relatively large burst sample to investigate astrometric accuracy and find that for $\gtrsim$20 baselines ($\gtrsim$7 dishes) we can robustly reach milliarcsecond precision even using single-burst data sets. Subarcsecond precision is still possible for single bursts, even when only $\sim$6 baselines (four dishes) are available. In such cases, the limited *uv* coverage for individual bursts results in very high side-lobe levels. Thus, in addition to the peak position from the dirty map, we also explore smoothing the structure in the dirty map by fitting Gaussian functions to the fringe pattern in order to constrain individual burst positions, which we find to be more reliable. Our VLBI work places FRB 20201124A 710 ± 30 mas (1σ uncertainty) from the optical center of the host galaxy, consistent with originating from within the recently discovered extended radio structure associated with star formation in the host galaxy. Future high-resolution optical observations, e.g., with Hubble Space Telescope, can determine the proximity of FRB 20201124A's position to nearby knots of star formation.

Unified Astronomy Thesaurus concepts: Radio astrometry (1337); Radio transient sources (2008); Very long baseline interferometry (1769)

1. Introduction

Fast radio bursts (FRBs) are highly luminous, short-duration coherent radio transients (for recent reviews, see Cordes & Chatterjee 2019; Petroff et al. 2019, 2021). The vast majority of the observed FRB population are apparently one-off events, but a few percent of the known FRBs have been seen to repeat. Whether all FRBs are capable of repeating, or if the observed FRB population comes from multiple origins, remains debatable. Nonetheless, the large sample provided by CHIME/FRB (CHIME/FRB Collaboration et al. 2018) shows statistical differences between the properties of apparent one-offs and repeaters (Pleunis et al. 2021a). The repeating sources are particularly valuable in our efforts to understand the nature of FRBs because they allow for follow-up observations to, e.g., explore their burst energy distribution (Gourdji et al. 2019; Hewitt et al. 2021; Li et al. 2021), characterize the evolution of the burst properties with time and frequency (Michilli et al. 2018a; Gajjar et al. 2018; Hilmarsson et al. 2021b; Pleunis et al. 2021b), and probe the immediate surroundings of the FRB source through precise localization with very long baseline interferometry (VLBI) and high-resolution optical imaging (Bassa et al. 2017; Mannings et al. 2021; Tendulkar et al. 2021).

To date, 19 FRBs have been localized with sufficient precision ($<$ a few arcseconds) to identify their host galaxy (e.g., Chatterjee et al. 2017; Bannister et al. 2019; Ravi et al. 2019; Heintz et al. 2020; Bhandari et al. 2021).[11] Thus far, only three of these are localized to 1–10 mas precision using VLBI (Marcote et al. 2017, 2020; Kirsten et al. 2022). With VLBI precision, the exact location of the FRB progenitor within the host galaxy can be determined and matched with any prominent features, like spiral arms, the galactic nucleus, or star-forming regions. This is particularly useful if the host can be resolved with Hubble Space Telescope observations (Bassa et al. 2017; Mannings et al. 2021; Tendulkar et al. 2021).

VLBI localizations of repeating FRBs have uncovered a diversity of local environments: FRB 20121102A, the first-known repeater, is spatially coincident with a compact persistent radio

[11] https://frbhosts.org/

source and inside a star-forming region in a dwarf host galaxy (Bassa et al. 2017; Chatterjee et al. 2017; Marcote et al. 2017; Tendulkar et al. 2017); FRB 20180916B is located in the spiral arm of a Milky Way–like host, approximately 250 pc from the peak of a prominent star-forming knot (Marcote et al. 2020; Tendulkar et al. 2021); and FRB 20200120E was discovered to be in a globular cluster that is associated with the grand-design spiral galaxy M81 (Bhardwaj et al. 2021; Kirsten et al. 2022). This diversity highlights that the progenitors of repeating FRBs are able to live in different types of environments or, alternatively, that there is more than one progenitor type for repeating FRBs. Additional VLBI FRB localizations, combined with comparably high-resolution optical and radio imaging, allow us to study the immediate environments of FRBs (e.g., a surrounding nebula) and to compare with other astronomical source classes. This will help uncover the full diversity of FRB local environments, giving insight into the FRB progenitor(s).

In this Letter, we present the European VLBI Network (EVN) localization of the repeating FRB 20201124A. FRB 20201124A was in a period of heightened activity in 2021 April (Chime/Frb Collaboration 2021), during which we detected a total of 18 bursts at two epochs. A preliminary EVN position was originally reported in Marcote et al. (2021), who used data only from the first epoch. Here, we describe in detail the interferometric observations (Section 2), followed by the analysis and results (Section 3). Because we detected a relatively large sample of bursts at two separate epochs, a first for FRB observations using the VLBI technique, we use this to test the astrometric accuracy of the method (Section 4). We investigate the astrometric accuracy for individual bursts and a low number of available antennas. Finally, we discuss our results in the context of recent studies of FRB 20201124A and other FRBs.

2. Observations

We observed FRB 20201124A on April 10 2021 15:00—21:00 UT (project ID pr153a) and April 19 2021 13:30—19:30 UT (project ID pr156a) as part of our ongoing FRB VLBI localization project, PRECISE (Pinpointing REpeating ChIme Sources with Evn dishes).[12] We used an ad hoc array of six and nine radio telescopes (that are also part of the EVN) on April 10 and 19, respectively. We pointed at the position derived from earlier Very Large Array (VLA) observations: R. A. (J2000) = $5^{h}08^{m}03.^{s}5$, decl. (J2000) = +26°03′37.″8 (Law et al. 2021). The telescopes that participated in our campaign were Onsala (On-85), Toruń Irbene, Westerbork single-dish RT1, Noto and Effelsberg at Epoch 1, and Onsala (On-85), Toruń Irbene, Westerbork single-dish RT1, Medicina, Svetloe, Badary, Sardinia, and Effelsberg at Epoch 2. The central observing frequency of our observations was 1.4 GHz, and the bandwidth and number of subbands were dependent on the capabilities at each station (see Table 1). Phase referencing was done with a cycle time of 6–8.5 minutes: 1.5–2.5 minutes on the phase calibrator source (J0502+2516, at a separation of 1.°4 from FRB 20201124A), followed by 4.5–6.5 minutes on target. We use the position of J0502+2516 reported in the rfc2018a catalog[13] during correlation: R.A. (J2000) = $5^{h}02^{m}58.^{s}474768$, decl. (J2000) = +25°16′25.″27549 (offset by 0.09 mas in R.A. and decl. from the rfc2021c catalog[14], i.e., within the listed uncertainty of 0.12 mas). Scans of J1048+7143 and J0555+3948 were taken to use as fringe finders and bandpass calibrators in the first and second epochs, respectively. Additionally, we observed the pulsar PSR J2257+5909 for 5 minutes per epoch to test the data quality of the single-dish data and frequent, phase-referenced scans of J0501+2530 to use as an interferometric check source. In total, we observed the target FRB 20201124A for 7.1 hr.

Table 1
Individual Telescope Configurations Used during Our Interferometric Observations

Telescope	Frequency coverage (MHz)	No. of Subbands	Epoch[a]
Effelsberg (Ef)	1254–1510	16 × 16 MHz	1,2
Onsala (O8)	1254–1510	16 × 16 MHz	1,2
Toruń (Tr)	1254–1510	16 × 16 MHz	1,2
Irbene (Ir)	1382–1510	8 × 16 MHz	1,2
Westerbork (Wb)	1382–1510	8 × 16 MHz	1,2
Noto (Nt)	1318–1574	16 × 16 MHz	1
Medicina (Mc)	1350–1478	8 × 16 MHz	2
Svetloe (Sv)	1382–1510	8 × 16 MHz	2
Badary (Bd)	1382–1510	8 × 16 MHz	2
Sardinia (Sr)	1350–1606	8 × 32 MHz	2

Note.
[a] Epochs during which the telescope participated, where Epoch 1 corresponds to EVN project code EK048D, and Epoch 2 is EK048E.

We recorded raw voltage data with dual circular polarization and 2 bit sampling from each telescope that participated, in either VDIF (Whitney et al. 2010) or MARK5B (in the case of Svetloe and Badary; Whitney 2004) format. In parallel, we simultaneously recorded pulsar backend data at Effelsberg during both epochs and at Sardinia during Epoch 2. At Effelsberg, total intensity filterbank data were recorded using the PSRIX pulsar backend (Lazarus et al. 2016). Unfortunately, the PSRIX data recorded on April 10 suffered from an incorrect observing setup and were not usable. The PSRIX data on April 19 were recorded with time and frequency resolutions of 102.4 μs and 0.49 MHz, respectively, and a usable frequency range of 1255–1505 MHz. At Sardinia, the pulsar data were recorded using the Digital Filterbank Mark III backend (DFB; Prandoni et al. 2017), in `psrfits` format (Hotan et al. 2004). These data have time and frequency resolutions of 128 μs and 1 MHz, respectively, and a frequency range of 1140.5–2163.5 MHz, of which 1210.5–1739.5 MHz is usable (given the receiver response and radio frequency interference).

3. Analysis and Results

3.1. Burst Discovery

For both Effelsberg and Sardinia, the raw voltage data and pulsar backend data were independently searched for bursts using distinct analysis pipelines. We converted the raw voltage data to filterbank format with a time and frequency resolution of 128 μs and 125 kHz, respectively, using `digifil` (van Straten & Bailes 2011). We used a Heimdall-based search to identify candidate FRBs, which were then classified using the machine-learning classifier FETCH (specifically, models A and H with a 50% probability threshold; Agarwal et al. 2020). In total, 27 candidates were identified by FETCH, of which 18 were deemed astrophysical in nature by human inspection: 13

[12] https://www.ira.inaf.it/precise/Home.html
[13] http://astrogeo.org/vlbi/solutions/rfc_2018a/
[14] http://astrogeo.org/sol/rfc/rfc_2021c/

bursts on April 10 (Epoch 1) and a further 5 on April 19 (Epoch 2).

A single-pulse search of the PSRIX and DFB data was conducted using PRESTO tools (Ransom 2001), including masking of radio frequency interference (RFI) using the `rfifind` tool. The candidate FRBs were then classified using an automated clustering classifier based on Michilli et al. (2018b). The data quality and analysis strategy were tested using a scan of the test pulsar PSR J2257+5909. We independently found all five bursts from Epoch 2 in the PSRIX data while only B14 was found in this way in the DFB data from Sardinia. The DFB data were additionally searched using a Spandak-based pipeline[15] (Gajjar et al. 2018, 2021), which discovered B15 and B16. Post-search analysis revealed that the other bursts were either below the signal-to-noise ratio (S/N) threshold of 7 used in the search or coincident with severe RFI and consequently ruled nonastrophysical by the classifier.

For the remainder of this Letter, the bursts are named B*n*, where *n* is an integer from 1 to 18, ordered according to the burst arrival time.

3.2. Localization

The interferometric data were correlated using the software correlator SFXC (Keimpema et al. 2015) at the Joint Institute for VLBI ERIC (JIVE; in the Netherlands), with an integration time of 2 s and 64 channels per 16 MHz subband (under the EVN correlation-only proposal EK048, PI: Kirsten). Using the arrival times of the 18 FRB 20201124A bursts detected during our PRECISE campaign, a second correlation was performed for only the data containing bursts, where the gate width used for correlation was determined by eye to maximize the S/N. These values are recorded in Table 2. The phase center used for correlation was the VLA FRB 20201124A localization position (Law et al. 2021), which has an uncertainty of approximately 1″. This meant that we were not required to correlate the data for a third time to move the phase center closer to the FRB position, as has been required in previous VLBI FRB projects (Marcote et al. 2020; Kirsten et al. 2022).

The analysis steps for interferometric calibration and imaging were performed using standard tasks in the Astronomical Image Processing System, `AIPS` (Greisen 2003) and `DIFMAP` (Shepherd et al. 1994). Initially, using the products from the automated EVN Pipeline,[16] we performed a priori amplitude calibration using the gain curves and system temperature measurements from each station. We also applied a bandpass calibration, in addition to some basic flagging when telescopes were off source. Burst B5 occurred while Effelsberg was still slewing, and so these data were flagged by this initial flagging step. Therefore, we removed these flags from the burst interferometric data to recover the data for burst B5. We note that B5 occurred at most a few seconds before Effelsberg was pointing at the exact VLA position of FRB 20201124A and therefore was only at most 10% of Effelsberg's half-power radius (270″ at 1.4 GHz) from the beam center. We conclude that the offset is too small to require an additional primary beam correction for this burst. At Epoch 1 (EVN correlation project code: EK048D, PRECISE observing code: pr153a), no fringes were detected from Irbene until 17:35 UT, and therefore there are no data from Irbene for bursts B1–B4. The station Badary had reduced time during Epoch 2 (EK048E, pr156a) and therefore did not observe after 15:45 UT, resulting in no data for this station during any of the bursts detected at Epoch 2. Delays due to dispersion in the ionosphere are corrected for using the Jet Propulsion Laboratory total electron content maps provided by CDDIS (Noll 2010). We first remove the instrumental delay, i.e., phase jumps between the subbands, using the bright calibrator sources J1048+7143 and J0555 +3948 for Epochs 1 and 2, respectively. Then we correct the phases for the entire observation, as a function of time and frequency, by performing a fringe fit using all calibrator sources. Throughout, we use the most sensitive dish, the 100 m Effelsberg telescope, as our reference antenna for calibration. During Epoch 2, the phase solutions for Irbene were rapidly varying, thus we conclude that the solutions applied to the target are unreliable, and we therefore flag these data. In Table 2, we report the "effective" number of baselines. This accounts for the stations that did not record data at the time of the burst; stations that were flagged during calibration; and, additionally, the loss of sensitivity due to the spectra of some bursts peaking in the lower part of the observing band of Effelsberg, where some telescopes did not observe (see Table 1 for frequency coverage per participating telescope and Figure 1 for the burst dynamic spectra).

The phase calibrator, J0502+2516, was then imaged using `DIFMAP`, independently for both epochs. During Epoch 1, the recovered flux from the phase calibrator was 0.179 Jy, while during Epoch 2, the flux had dropped to 0.102 Jy, and the clean image exhibited strong side lobes, which we attribute to persistent amplitude errors after calibration. Additionally, radio maps of J0502+2154 from 2018 December at 5 GHz and 8.6 GHz exhibit an unresolved flux of ∼0.18 Jy,[17] allowing us to assume our higher measured flux is the true value. We therefore use a model of J0502+2516 determined using the data from Epoch 1 to self-calibrate the data from both epochs. This is an appropriate step because the active galactic nucleus (AGN) J0502+2516 is not expected to vary in brightness significantly on ∼ week timescales. The self-calibrated peak brightness of the phase calibrator is 0.178 Jy beam^{-1} and 0.179 Jy beam^{-1} for Epochs 1 and 2, respectively. The self-calibration solutions were then transferred to the target, before imaging. Throughout this work we make images of size 8192 × 8192, with 1 mas pixels.

In Figure 2 (left), we plot the clean 1.4 GHz map of all 18 bursts presented in this work. The combined *uv* coverage of all 18 bursts results in a synthesized beam with major axis 37.3 mas, minor axis 17.98 mas, and position angle of 55.°85. The clean map is produced by fitting a Gaussian component to the visibilities in the *uv* plane and inverse Fourier-transforming using `DIFMAP`'s `modelfit` tool. The combined visibilities from all bursts provide us with the best available *uv* coverage and so from this we derive the J2000 position of FRB 20201124Ain the International Celestial Reference Frame (ICRF): R. A. = $05^{h}08^{m}03.^{s}5074 \pm 2.7$ mas, decl. = $+26°03'38.''5052 \pm 2.6$ mas. The peak emission is 24σ compared to the image noise, with the next-highest side lobes measured at approximately 30% of the peak value. We note that the interferometric image S/N per individual burst (Table 2) is in general lower than the Effelsberg single-dish S/N (Table 3) per burst. The time-domain S/N is computed using off-burst data

[15] https://github.com/gajjarv/PulsarSearch
[16] https://evlbi.org/evn-data-access
[17] http://astrogeo.org/cgi-bin/imdb_get_source.csh?source_name=J0502%2B2516

Table 2
Interferometric Burst Properties

Burst	Peak Position[a] (R.A., Decl. (J2000))	Gaussian Position[b] (R.A., Decl. (J2000))	σ_{maj}[c] (mas)	σ_{min}[d] (mas)	θ[e] (deg)	Peak Flux Density[f] (Jy/beam)	S/N[g]	Gate Width (ms)	Effective No. of Baselines[h]
Epoch 1									
B1	$05^h08^m03\overset{s}{.}5070$, $+26°03'38\overset{''}{.}503$	$05^h08^m03\overset{s}{.}5099$, $+26°03'38\overset{''}{.}5068$	496.1	196.5	46.4	0.34 ± 0.06	11.3	4.12	10
B2	$05^h08^m03\overset{s}{.}5073$, $+26°0'38\overset{''}{.}504$	$05^h08^m03\overset{s}{.}5133$, $+26°0'38\overset{''}{.}4931$	731.9	331.5	52.5	0.65 ± 0.05	13.8	8.49	10
B3	$05^h08^m03\overset{s}{.}4865$, $+26°0'38\overset{''}{.}601$	$05^h08^m03\overset{s}{.}4997$, $+26°0'38\overset{''}{.}5736$	1029.9	498.5	55.8	0.19 ± 0.04	5.2	4.02	6
B4	$05^h08^m03\overset{s}{.}5170$, $+26°0'38\overset{''}{.}441$	$05^h08^m03\overset{s}{.}5112$, $+26°0'38\overset{''}{.}5055$	773.1	353.3	55.8	0.32 ± 0.05	7.4	5.15	6
B5	$05^h08^m03\overset{s}{.}5140$, $+26°0'38\overset{''}{.}529$	$05^h08^m03\overset{s}{.}5097$, $+26°0'38\overset{''}{.}5686$	624.6	270.7	89.9	0.24 ± 0.03	10.7	7.50	6
B6	$05^h08^m03\overset{s}{.}5068$, $+26°0'38\overset{''}{.}504$	$05^h08^m03\overset{s}{.}5079$, $+26°0'38\overset{''}{.}4960$	762.3	324.8	105.6	0.95 ± 0.06	13.5	14.54	15
B7	$05^h08^m03\overset{s}{.}4822$, $+26°0'38\overset{''}{.}482$	$05^h08^m03\overset{s}{.}5155$, $+26°0'38\overset{''}{.}5333$	1203.2	487.3	110.8	0.33 ± 0.05	7.3	3.78	6
B8	$05^h08^m03\overset{s}{.}5063$, $+26°0'38\overset{''}{.}496$	$05^h08^m03\overset{s}{.}5076$, $+26°0'38\overset{''}{.}4971$	1267.3	382.9	114.4	0.54 ± 0.06	13.4	10.75	6
B9	$05^h08^m03\overset{s}{.}5102$, $+26°0'38\overset{''}{.}229$	$05^h08^m03\overset{s}{.}5046$, $+26°0'38\overset{''}{.}4606$	1535.8	611.9	109.0	0.23 ± 0.04	9.2	8.47	6
B10	$05^h08^m03\overset{s}{.}5290$, $+26°0'38\overset{''}{.}985$	$05^h08^m03\overset{s}{.}5148$, $+26°0'38\overset{''}{.}8008$	1088.9	334.2	118.2	0.21 ± 0.03	7.7	6.01	6
B11	$05^h08^m03\overset{s}{.}5097$, $+26°0'38\overset{''}{.}519$	$05^h08^m03\overset{s}{.}5062$, $+26°0'38\overset{''}{.}4736$	1327.6	274.1	128.2	1.29 ± 0.20	16.6	10.56	15
B12	$05^h08^m03\overset{s}{.}4839$, $+26°0'38\overset{''}{.}661$	…	…	…	…	0.17 ± 0.03	4.3	5.12	15
B13	$05^h08^m03\overset{s}{.}5509$, $+26°0'39\overset{''}{.}034$	…	…	…	…	0.67 ± 0.06	13.3	8.18	6
Epoch 2									
B14	$05^h08^m03\overset{s}{.}5076$, $+26°0'38\overset{''}{.}507$	$05^h08^m03\overset{s}{.}5071$, $+26°0'38\overset{''}{.}4802$	530.1	249.9	105.6	0.79 ± 0.05	21.8	9.44	21
B15	$05^h08^m03\overset{s}{.}5076$, $+26°0'38\overset{''}{.}509$	$05^h08^m03\overset{s}{.}5059$, $+26°0'38\overset{''}{.}4744$	450.9	235.8	108.0	1.27 ± 0.10	12.6	3.14	21
B16	$05^h08^m03\overset{s}{.}5072$, $+26°0'38\overset{''}{.}509$	$05^h08^m03\overset{s}{.}5072$, $+26°0'38\overset{''}{.}4593$	503.0	198.4	119.8	0.61 ± 0.06	9.9	6.54	21
B17	$05^h08^m03\overset{s}{.}5072$, $+26°0'38\overset{''}{.}508$	$05^h08^m03\overset{s}{.}5106$, $+26°0'38\overset{''}{.}4852$	665.5	238.6	125.1	0.42 ± 0.03	16.4	7.07	21
B18	$05^h08^m03\overset{s}{.}5075$, $+26°0'38\overset{''}{.}511$	…	…	…	…	0.37 ± 0.04	8.7	5.52	21

Notes.
[a] Position of the intensity peak on the dirty map.
[b] Centroid of the two-dimensional Gaussian fit to the intersection of the cross-fringe pattern in the dirty map.
[c] The 1σ major axis of the Gaussian.
[d] The 1σ minor axis of the Gaussian.
[e] The rotational angle of the Gaussian. Measured anticlockwise.
[f] Determined using the peak of the individual burst dirty maps.
[g] S/N of the clean maps per individual burst, where the clean maps are generated by fitting a circular Gaussian to the visibilities and inverse Fourier-transforming using `DIFMAP`'s `modelfit` tool.
[h] As is clear in Figure 1, some bursts are narrow band with emission mainly below 1380 MHz. Some of the participating telescopes did not observe the lower frequencies (Table 1) and therefore have reduced sensitivity to these bursts. The "effective" number of baselines is including only the telescopes where the burst emission falls significantly within the observing band.

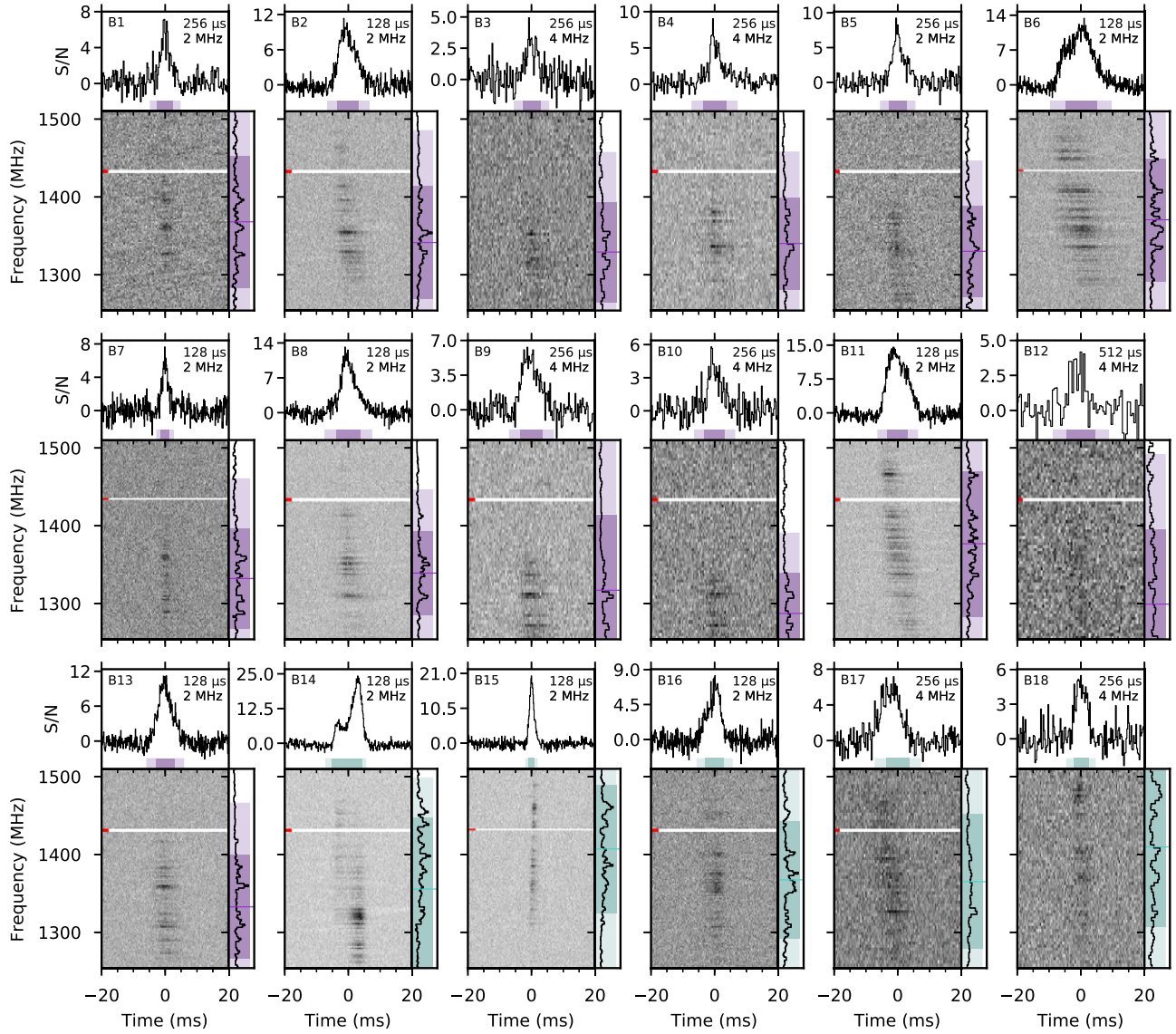

Figure 1. Dynamic spectra, temporal profiles, and time-averaged spectra for all 18 bursts presented in this work. For each subfigure, the burst name and time/frequency resolution are shown in the top left and top right, respectively. The colored bars represent the 1σ (dark) and 2σ (light) regions of the temporal width and spectral extent of each burst. Purple is used for bursts detected during Epoch 1, and cyan for those detected during Epoch 2. Data that have been masked due to radio frequency interference is not plotted and indicated with the red ticks. Each burst has been dedispersed using a dispersion measure of 412 pc cm^{-3}.

(data with only instrumental noise and no signal), whereas the noise properties of the interferometric data are influenced by the signal itself and contain strong residuals that become more prominent with brighter signals and lower *uv* coverage. The combined image S/N (24σ) is lower than the expected combination of the individual burst S/N values (Table 2; quadrature sum is 51.2). This likely arises due to this dynamic range issue described above and possibly also coherence loss when combining the individual bursts.

Additionally, we applied the same outlined calibration steps to the check source J0501+2530 and recovered the source with positional offset ΔR.A. $= 1.5$ mas, Δdecl. $= 0.6$ mas from the expected position (as quoted in the rfc2021c catalog[18]). The localization of FRB 20201124A is therefore robust. The uncertainties on the final position of FRB 20201124A are the quadrature sum of the statistical uncertainties derived from the shape and size of the synthesized beam, normalized by the S/N (ΔR.A. $= 0.7$ mas, Δdecl. $= 0.4$ mas), the statistical uncertainty on the phase calibrator position (± 0.13 mas), an estimate of the systematic uncertainty due to the separation of the phase calibrator and target (conservatively ± 2.5 mas; Kirsten et al. 2015), and an estimate of the frequency-dependent shift in the phase calibrator position from the ICRF (conservatively $\pm$ 1 mas; Plavin et al. 2019). The position of FRB 20201124A reported here is in agreement (within 2σ) of the original EVN localization reported in Marcote et al. (2021), which was determined using only the burst data from Epoch 1. Our position for FRB 20201124A is also in agreement with the independent measurements of the VLA (Ravi et al. 2021), the Australian Square Kilometre Array Pathfinder (ASKAP) (Fong et al. 2021), and the upgraded Giant Metrewave Radio Telescope (uGMRT; if one includes the estimated systematic uncertainties they discuss; Wharton et al. 2021a). These studies are approximately two to three orders of magnitude less precise

[18] http://astrogeo.org/sol/rfc/rfc_2021c/

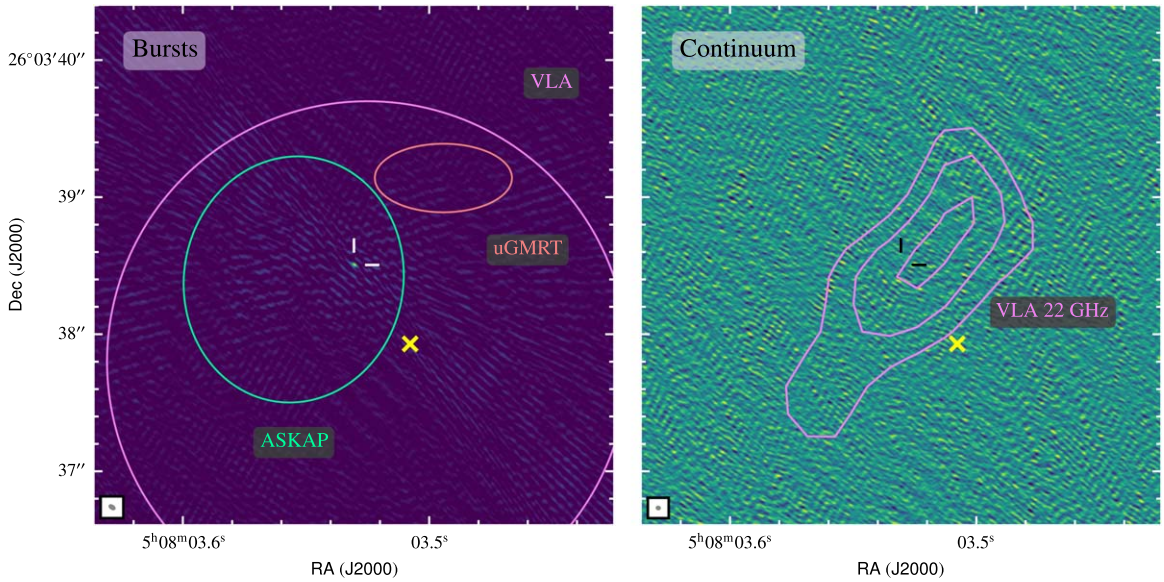

Figure 2. Left panel: clean EVN 1.4 GHz map of the combined visibilities of all 18 bursts detected during both epochs (i.e., the inverse Fourier transform of the visibilities after deconvolving the telescope response). The white ticks indicate the position of FRB 20201124A. The localization regions of FRB 20201124A as reported by VLA (Ravi et al. 2021), ASKAP (Fong et al. 2021), and uGMRT (Wharton et al. 2021a) are overplotted using pink, green, and orange lines, respectively. Right panel: dirty EVN map (before deconvolution of the interferometer response) of all continuum target data from both epochs to search for persistent radio emission. The position of FRB 20201124A is indicated by the black ticks. Overplotted are the 3σ, 4σ, and 5σ contours of the resolved radio emission detected by the VLA at 22 GHz (Piro et al. 2021). In both panels, the optical center of the host galaxy is indicated by the yellow cross (Fong et al. 2021). The synthesized beam is shown at the bottom left of each panel. Both maps are made using a natural weighting scheme.

Table 3
Burst Properties from Effelsberg Single-dish Data

Burst	Time of Arrival[a] (MJD)	Fluence[c] (Jy ms)	S/N[c]	Peak Flux Density[b] (Jy)	Spectral Luminosity[d] (10^{31} erg s^{-1} Hz^{-1})	Width[e] (ms)	Frequency Extent[e] (MHz)	Scintillation Bandwidth[f] (MHz)
Epoch 1								
B1	59314.63581536	0.94 ± 0.19	13.9	0.31 ± 0.06	2.38 ± 0.48	4.0 ± 0.3	141.1 ± 0.5	3.0 ± 0.7
B2	59314.67002510	3.68 ± 0.74	44.1	0.73 ± 0.15	6.78 ± 1.36	5.6 ± 0.1	120.2 ± 0.1	2.2 ± 0.3
B3	59314.69180857	0.61 ± 0.12	7.5	0.24 ± 0.05	1.34 ± 0.27	4.7 ± 0.1	107.1 ± 0.7	2.8 ± 1.1
B4	59314.71490874	1.49 ± 0.30	16.3	0.43 ± 0.09	2.56 ± 0.51	6.0 ± 0.1	98.4 ± 0.2	2.5 ± 0.6
B5	59314.75153586	1.53 ± 0.31	18.2	0.46 ± 0.09	0.33 ± 0.67	4.7 ± 0.2	97.2 ± 0.3	2.3 ± 0.6
B6	59314.79580654	6.50 ± 1.30	67.9	0.91 ± 0.16	8.20 ± 1.64	8.1 ± 0.1	131.4 ± 0.1	1.9 ± 0.3
B7	59314.80440853	0.94 ± 0.19	16.4	0.52 ± 0.10	4.11 ± 0.82	2.4 ± 0.1	107.3 ± 0.2	2.8 ± 0.5
B8	59314.82591958	4.48 ± 0.90	46.1	0.92 ± 0.18	7.29 ± 1.26	6.3 ± 0.1	89.6 ± 0.1	2.3 ± 0.5
B9	59314.83037838	1.40 ± 0.28	17.0	0.27 ± 0.05	2.40 ± 0.48	5.9 ± 0.1	81.2 ± 0.1	2.0 ± 0.5
B10	59314.84159434	1.31 ± 0.26	12.4	0.34 ± 0.07	2.51 ± 0.50	5.4 ± 0.3	86.4 ± 0.5	3.4 ± 0.9
B11	59314.85888953	5.92 ± 1.18	76.0	0.89 ± 0.18	11.4 ± 2.3	5.3 ± 0.1	155.3 ± 0.1	1.3 ± 0.3
B12	59314.86388348	0.63 ± 0.13	6.7	0.13 ± 0.03	0.88 ± 0.18	7.4 ± 1.1	160.6 ± 0.7	⋯
B13	59314.87198956	3.39 ± 0.68	41.2	0.75 ± 0.15	6.98 ± 1.40	5.0 ± 0.1	111.4 ± 0.1	2.1 ± 0.4
Epoch 2								
B14[g]	59323.65617164	6.56 ± 1.31	82.1	1.51 ± 0.15	12.5 ± 2.5	2.3 ± 0.1 3.6 ± 0.1	129.8 ± 0.2 86.9 ± 0.1	1.1 ± 0.3
B15	59323.66919992	1.98 ± 0.40	46.3	1.23 ± 0.25	12.6 ± 2.5	1.6 ± 0.1	136.7 ± 0.1	1.7 ± 0.3
B16	59323.71603797	1.95 ± 0.39	26.3	0.5 ± 0.1	4.15 ± 0.83	4.8 ± 0.1	125.5 ± 0.1	3.3 ± 0.6
B17	59323.74152501	1.78 ± 0.36	21.2	0.31 ± 0.06	2.94 ± 0.59	6.1 ± 0.1	143.6 ± 0.2	1.1 ± 0.4
B18	59323.79497897	0.91 ± 0.18	13.8	0.24 ± 0.05	2.43 ± 0.49	3.9 ± 0.1	170.8 ± 0.6	1.3 ± 0.6

Notes.
[a] Corrected to the Solar System Barycenter to infinite frequency assuming a dispersion measure of 412 pc cm^{-3}, reference frequency 1502 MHz, and dispersion constant of $1/(2.41 \times 10^{-4})$ MHz^2 pc^{-1} cm^3 s. The times quoted are dynamical times (TDB).
[b] We estimate a conservative 20% uncertainty on these measurements, arising due to the uncertainty in the system equivalent flux density (SEFD) of Effelsberg.
[c] Boxcar S/N. Defined as the sum of the burst in S/N units within the 2σ uncertainty region of the width and spectral extent, normalized by the 2σ width in time bins.
[d] Taking the luminosity distance of FRB 20201124A as 453 Mpc (Hilmarsson et al. 2021a; Day et al. 2021; Kilpatrick et al. 2021).
[e] FWHM of the Gaussian fit to the autocorrelation function of the dynamic spectrum.
[f] The uncertainty on the scintillation bandwidth is the quadrature sum of the fit uncertainties and $1/\sqrt{N_{\rm scint}}$, where $N_{\rm scint}$ is the approximate number of scintles.
[g] B14 has two visible components.

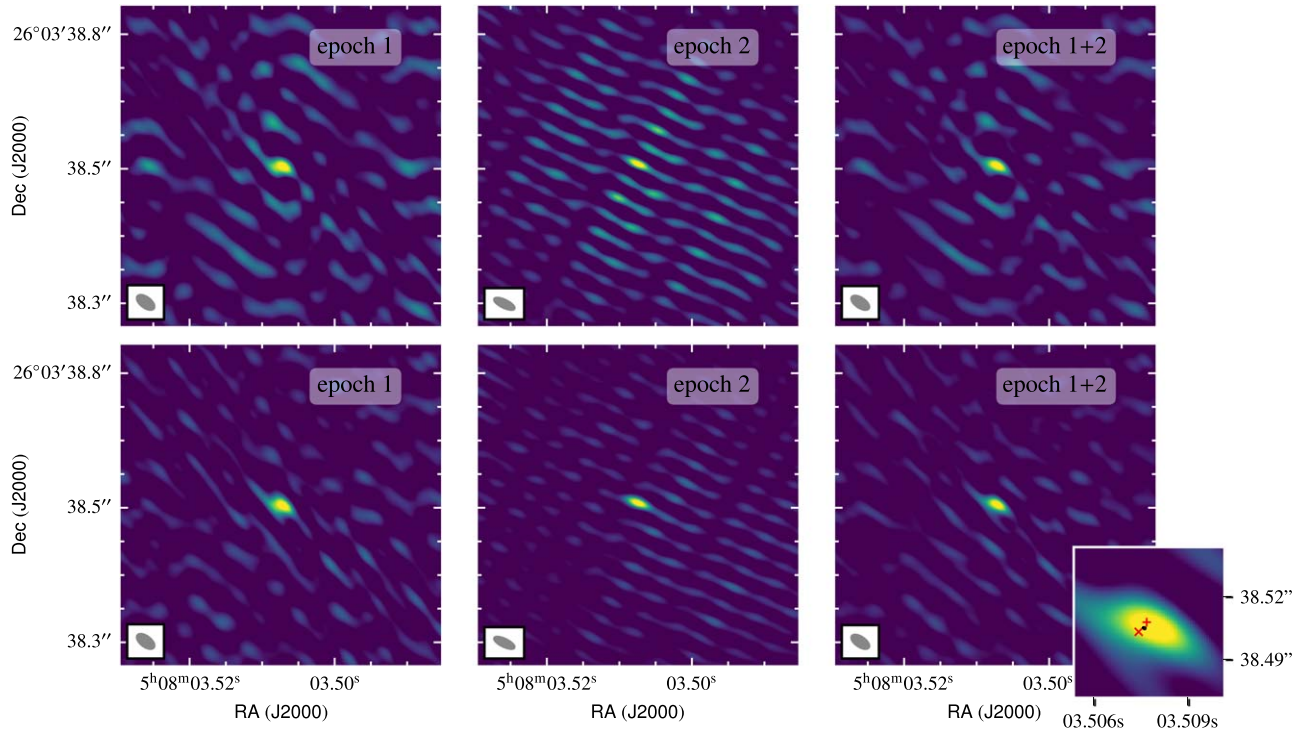

Figure 3. Top row: dirty maps (i.e., the inverse Fourier transform of the visibilities) of the combined visibilities of the 13 bursts discovered during Epoch 1 (left), the 5 bursts during Epoch 2 (middle), and all bursts from both epochs (right). Bottom row: same as the top row except showing clean maps (i.e., the Fourier transform of the visibilities after deconvolving the telescope response). The zoom-in panel on the bottom-right subplot shows the best-fit two-epoch position in black, with the positions from Epochs 1 and 2 independently represented by the red cross and plus, respectively. All images are made using a natural weighting scheme, and the scaling of each radio map goes from 5% to 85% of the peak value. The synthesized beam is shown at the bottom left of each panel.

than the localization presented here, however (a comparison is shown in Figure 2).

Additionally, we produced the dirty map of the entire ∼7 hr of target data from both epochs to search for any compact persistent radio emission at the site of the FRB or nearby (Figure 2, right). The rms noise in the continuum map, using a natural weighting scheme (using `uvweight` in `DIFMAP`) is 14 μJy beam^{-1}, and using a uniform weighting scheme is 25 μJy beam^{-1}. In addition, we tried applying different Gaussian tapers, 1, 2, and 5 Mλ (using `uvtaper` in `DIFMAP`) to downweight the longer baselines and hence boosting any possible extended emission. We find no significant persistent radio source above 6σ in an area of $8'' \times 8''$ around the FRB. This is in agreement with the original report in Marcote et al. (2021) and follow-up efforts with the Very Long Baseline Array (VLBA; Ravi et al. 2021). The shortest baseline in our array is ∼270 km, between Effelsberg and Westerbork, and thus emission above an angular scale of ∼160 mas is resolved out.

3.3. Burst Characterization

The data were coherently dedispersed to a dispersion measure (DM) of 413 pc cm^{-3} (Chime/Frb Collaboration 2021). We created 32 bit total intensity filterbank data for each burst by autocorrelating the single-dish Effelsberg raw voltage data using SFXC. These data have time and frequency resolutions of 8 μs and 125 kHz, respectively. We then created archive files using `PSRCHIVE` (Hotan et al. 2004), which have the same resolution as the filterbank data. The dynamic spectra, time profiles, and time-averaged spectra for all bursts are shown in Figure 1. We further refined the DM by optimizing the frequency-averaged structure (using `DM_phase`[19]) of burst B14, which exhibits a clear burst structure, to measure a DM of 412.2 ± 0.6 pc cm^{-3}. Additionally, using B15, which does not exhibit a clear structure but is the narrowest burst in our sample, we measure a DM of 411.6 ± 0.4 pc cm^{-3}. Note that for B15, using `DM phase` essentially maximizes the S/N because it does not exhibit clear burst structure. The final DM, which we used to incoherently shift the frequency channels for all bursts in our sample, assuming the DM does not vary significantly on <10 day timescales, was determined by averaging the two measurements: DM $= 412.0 \pm 0.7$ pc cm^{-3}.

To measure the temporal and spectral extent of the bursts, we performed a two-dimensional autocorrelation of each dynamic spectrum. The time of arrival and central frequency of the bursts were determined using a two-dimensional Gaussian fit to the dynamic spectrum. This method of peak and width determination is explained in more detail in Nimmo et al. (2022), and the values for the bursts in this work are reported in Table 3.

Within the 2σ burst width and spectral extent, indicated by the light-purple and light-cyan bars in Figure 1, we compute the burst fluence using the radiometer equation (Cordes & McLaughlin 2003). For this, we use the typical Effelsberg system temperature, 20 K, combined with a cosmic microwave background contribution of 3 K, and a sky background temperature of 1 K, which we obtain by extrapolating from the 408 MHz sky map (Remazeilles et al. 2015) using a spectral index of −2.7 (Reich & Reich 1988). We also use the typical Effelsberg gain of 1.54 Jy K^{-1}. The typical system values for

[19] https://github.com/danielemichilli/DM_phase.git

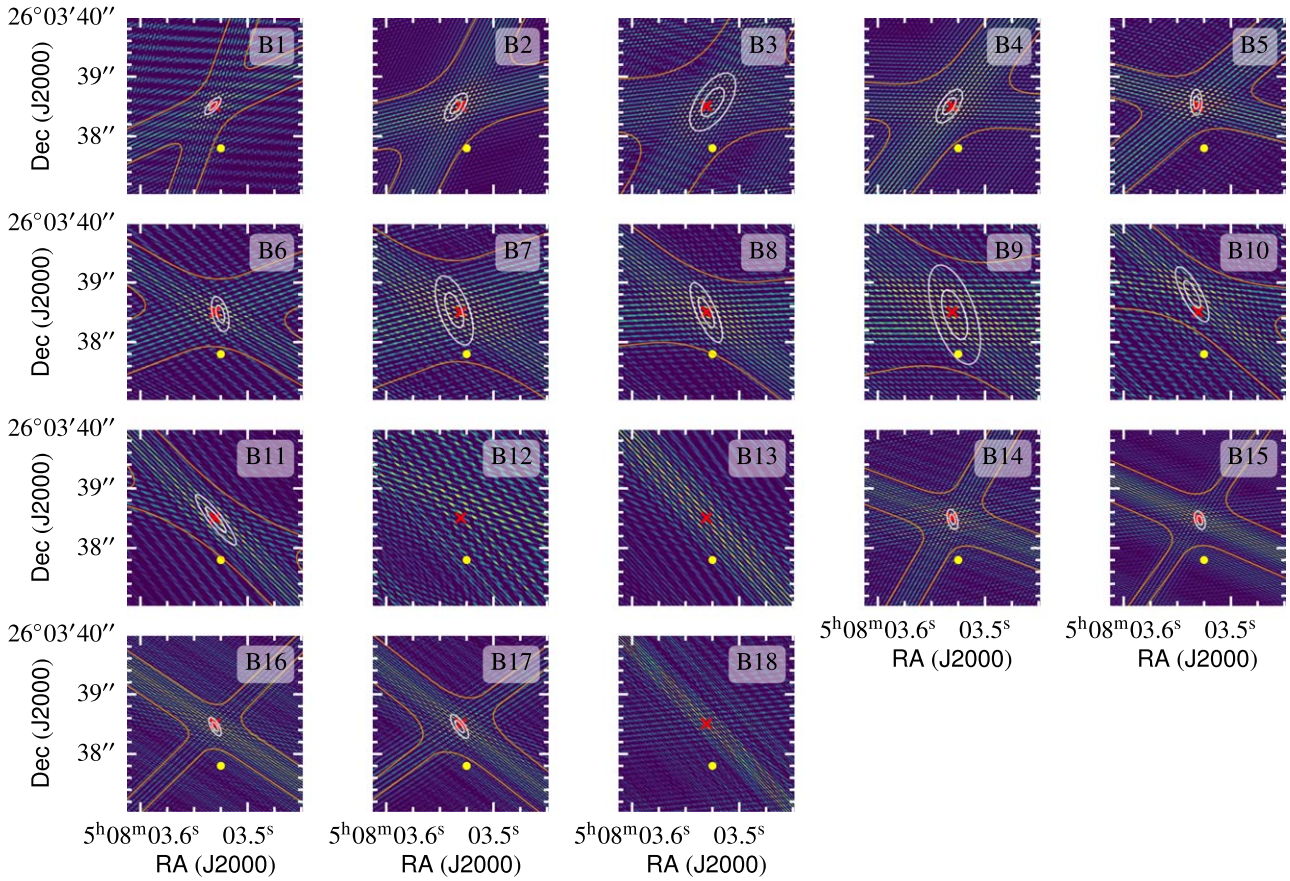

Figure 4. Dirty maps of the individual bursts, with the burst name shown at the top-right corner of each panel. The orange contours represent the two two-dimensional Gaussian fit (1σ region) to the cross-fringe pattern. The white contours represent the 1σ and 2σ Gaussian fits to the intersection of the double Gaussian, normalized by the S/N of the double Gaussian peak. Note: B12, B13, and B18 do not have a constraining Gaussian fit due to the lack of a cross pattern in the dirty map. The best-fit FRB 20201124A position using all 18 bursts is shown by the red cross on each panel, and the phase center used for correlation is indicated by the yellow point.

Effelsberg are uncertain on the 20% level, dominating the uncertainty on the fluence and peak flux density measurements reported in Table 3.

We computed the one-dimensional autocorrelation function (ACF) of the burst spectra in order to measure the scintillation bandwidth. The scintillation bandwidth is defined as the half-width at half-maximum of a Lorentzian fit to the ACF of the spectrum. We note that the zero-lag noise spike is removed from each ACF. Additionally, we subtract the off-burst ACF to reduce the power at low lags due to noise. The narrowbandedness of many of the bursts in our sample results in an additional frequency structure in the ACF with a characteristic bandwidth related to that of the frequency extent of the burst. For all bursts, other than B1, B15, B17, and B18, this broadband feature is visible in the ACF. We fit a one-dimensional Gaussian function to this wider component and subtract it from the ACF in order to disentangle the two frequency scales. Finally, we fit a Lorentzian function to the remaining structure in the ACF and measure the scintillation bandwidth per burst (reported in Table 3), which we find to be consistent with the results presented in Main et al. (2022).

4. Discussion

4.1. Astrometry

The final position of FRB 20201124A is determined from a combined image of all 18 bursts presented in this work. The combination of many bursts, at two epochs, maximizes the *uv* coverage. We also investigate the position of FRB 20201124A per observing epoch, in order to explore how consistent the FRB position is with an independent calibration, and observed on separate days. The position of FRB 20201124A using the combined visibilities of 13 bursts at Epoch 1 is R. A. $= 05^{h}08^{m}03.^{s}5076 \pm 2.8$ mas, decl. $= +26°03'38.''5035 \pm 2.8$ mas (following the error determination described in Section 3.2, with a resulting S/N of 16.8, and using the Epoch 1 beam shape). Similarly, the position of FRB 20201124A using the combined visibilities of five bursts at Epoch 2 is R. A. $= 05^{h}08^{m}03.^{s}5073 \pm 2.9$ mas, decl. $= +26°03'38.''5081 \pm 2.7$ mas (Epoch 2, S/N 18.5). Both per-epoch positions agree with the combined-epoch final position and with each other, within 2σ. In Figure 3, we plot the dirty maps (i.e., the inverse Fourier transform of the visibilities) of the combined visibilities from all 13 bursts in Epoch 1, the combined visibilities from all five bursts in Epoch 2, and the combined visibilities of all bursts from both epochs. Also shown in Figure 3 are the corresponding clean maps, with a visual comparison of the astrometry per epoch.

To explore the astrometry further, we determine the positions of each burst individually, using both the peak positions on the dirty map (dominated by the long baselines in the array) and Gaussian fits to the envelope of the fringe pattern (shown in Figure 4; dominated by the short baselines). We note that due to the lack of *uv* coverage per individual burst (Figure 5), the peak side-lobe level in the dirty map is on average 97% of the main lobe and in the worst case is >99%. This creates

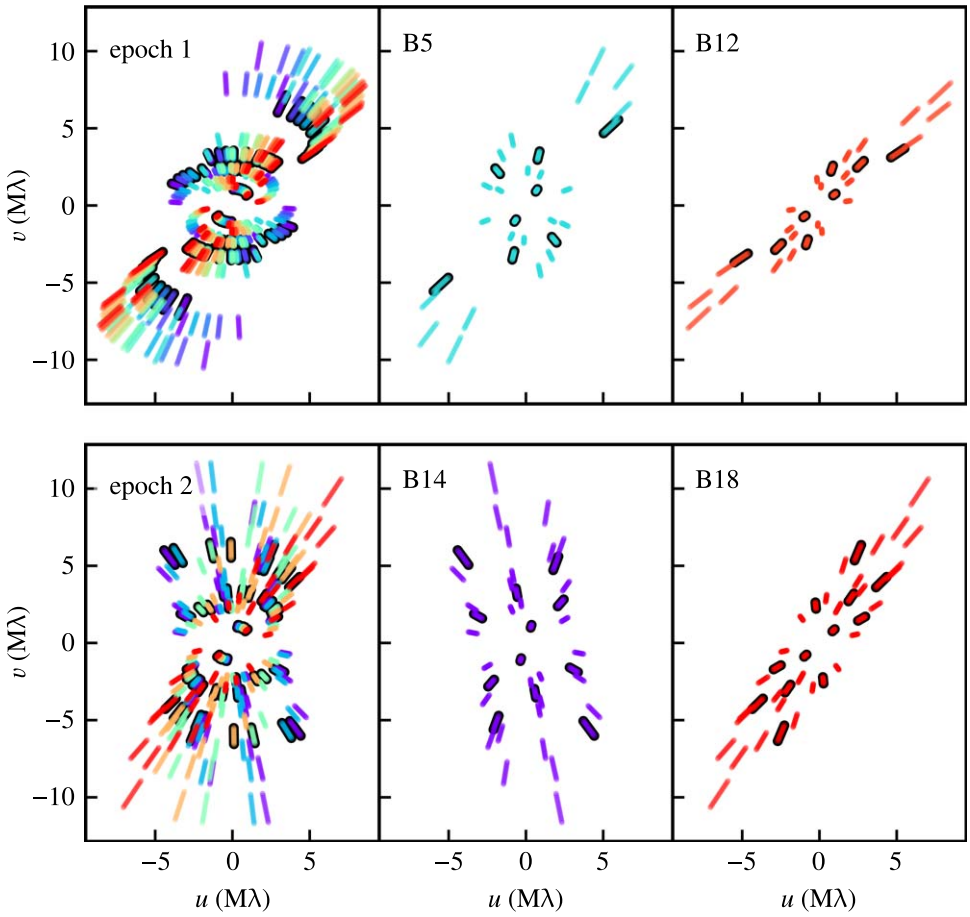

Figure 5. *uv* coverage per observing epoch (left panels) and *uv* coverage for representative individual bursts with (middle panels) and without (right panels) the cross-fringe pattern in the dirty map. The different colors represent individual bursts. There are multiple points plotted per baseline, representing the different frequency subbands. The points highlighted with the black outline represent baselines involving the Effelsberg telescope (the telescope with the highest sensitivity in our array), which dominates the structure seen in the dirty maps (Figure 4). For the representative individual bursts, the burst name is shown in the top left of the panel.

ambiguity in the individual burst positions, at a level comparable to the spacing between side lobes. This was also evident and discussed in the case of the VLBI localization of FRB 20121102A (Marcote et al. 2017) and highlights the need for an alternative approach. As an alternative approach, we fit smooth Gaussian functions to the dirty map pattern fringe pattern: we first fit two-dimensional Gaussians to both arms of the cross pattern in the fringes and then fit a single two-dimensional Gaussian to their intersection. Note that we include the Gaussian fits only for bursts that exhibit a clear cross-fringe pattern in their dirty map (Figure 4), which arises because the dirty map is dominated by baselines involving the Effelsberg telescope which span two primary axes in the *uv*-space (Figure 5). A Gaussian is not necessarily the optimal function to fit to the dirty map (the true function is dependent on the *uv* coverage). However, it is clear from the two two-dimensional Gaussian fits in Figure 4 and the fact that >68% of the 1σ Gaussians in Figure 6 intersect with the position of FRB 20201124A that this is a conservative approach to measure the intersection of the cross-fringe pattern and to account for the ambiguity of the burst position at the level of the side-lobe spacing.

The positions using both the peak and Gaussian-fit methods are reported in Table 2 and illustrated in Figure 6. In Figure 7, we show the separation of the peak and Gaussian positions per burst, from the best-fit position of FRB 20201124A. As a result of the larger number of baselines ($=N(N-1)/2=21$, for a number of telescopes N) during the second epoch, compared with the first, the peak positions of the Epoch 2 bursts agree within 10 mas of the true position. For the bursts from Epoch 1 (for which we have a lower number of baselines), the scatter in the peak positions increases and deviates farther from the true position, as expected. Accurately determining the astrometric uncertainty on the individual peak positions in the regime of the low number of baselines would likely require an empirical statistical study similar to Martí-Vidal et al. (2010b). However, based on Figure 7, an arcsecond localization is feasible given one burst above a detectability threshold of Fluence/$\sqrt{\text{Width}}$ ≈ 0.3 Jy ms$^{-1/2}$ (Marcote et al. 2017), detected with only six baselines (four telescopes).

By looking at the phases of the visibilities of the individual bursts, there is a clear scatter between approximately 50° and 100°. This scatter arises due to a combination of phase noise, and errors in phase referencing. The phase uncertainty from phase noise, $\Delta\phi_{\text{noise}}$, is related to the S/N as $\Delta\phi_{\text{noise}} = \frac{1}{\text{S/N}}$, for sufficient S/N (note that for small S/N this approximation does not hold; Crane & Napier 1989). The uncertainty on the phase referencing accuracy arises due to a combination of separation of phase calibrator and target, atmospheric conditions, and accuracy of the correlation model. Martí-Vidal et al. (2010a, 2010b) derive expressions to estimate VLBI

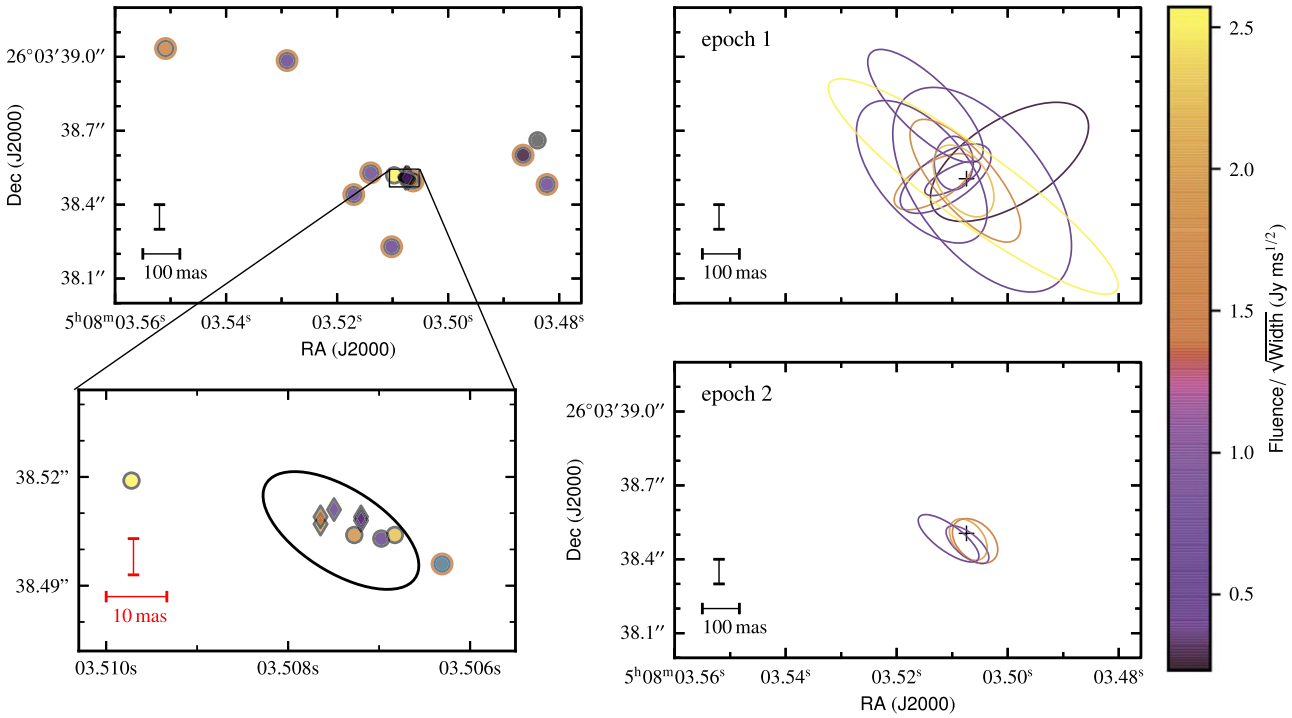

Figure 6. Individual burst positions determined using the intensity peak on the dirty maps (left) and a Gaussian fit to the dirty maps, which exhibit a clear cross-fringe pattern (right; see also Figure 4). Circles indicate bursts from Epoch 1 and diamonds bursts from Epoch 2. The color bar represents the burst fluence divided by the square root of the burst width and is used as a measure of the burst detectability (a proxy for S/N; Marcote et al. 2017). The black bars represent a 100 mas angular scale, while the red bars in the zoom-in panel represent a 10 mas angular scale. The black ellipse on the left-bottom plot represents the synthesized beam centered on the best-fit FRB 20201124A position, while the cross on the right plots represents the best-fit FRB 20201124A position (in both cases, using all 18 bursts). The points on the left plot outlined in red indicate the bursts that were detected with only six baselines, highlighting the impact of the low number of baselines on the scatter of individual burst positions.

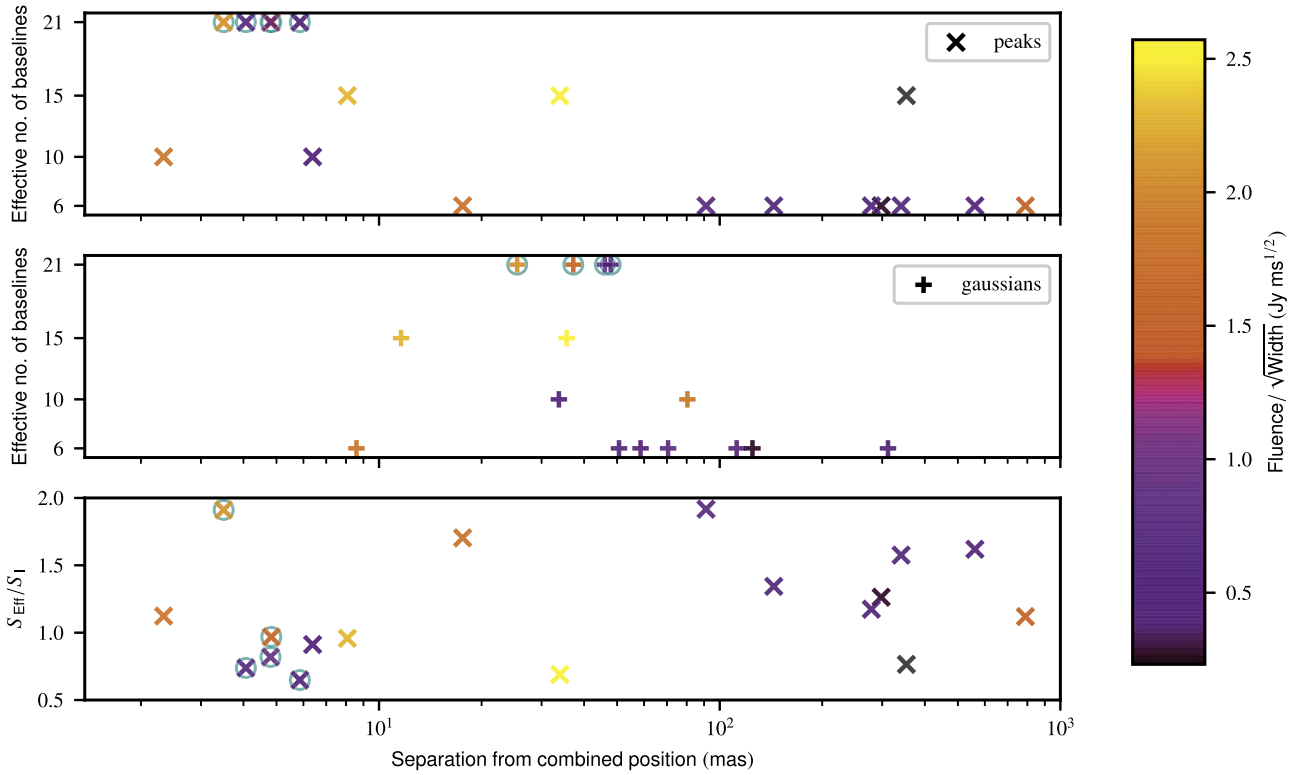

Figure 7. Separation of the peak (top) and Gaussian-fit (middle) positions of the individual bursts as presented in Figure 6, from the best-fit FRB 20201124A position (using all 18 bursts)—as a function of the effective number of baselines (defined in the text) and the detectability parameter Fluence/$\sqrt{\text{Width}}$. The bottom panel shows the separation of the peak individual burst positions from the best-fit FRB 20201124A position as a function of the burst peak flux density measured in the Effelsberg single-dish data (S_{Eff}) divided by that measured in the interferometric data (S_{I}). On all panels, the markers with the cyan circles indicate the bursts from Epoch 2.

astrometric uncertainties depending on the separation of the phase calibrator and target, observing frequency, integration time, and the telescope's diffraction limit. Although this approach allows for the negligible integration time for individual bursts, the small number of baselines will have a significant effect on the astrometric accuracy in this limiting case. Therefore, the expressions for astrometric accuracy derived in Martí-Vidal et al. (2010a, 2010b) will underestimate the uncertainties on the astrometry of individual bursts in this work, due to the lack of *uv* coverage. Assuming we have a realistic phase uncertainty, in our sparse *uv* coverage example, of 80°, arising from a combination of phase noise and calibration uncertainty, the expected positional shift of the fringe pattern is $\sim 1.22\lambda/b \times 100/180 \approx 89$ mas, where λ is our central observing wavelength and b in this case is the shortest baseline of 270 km between Effelsberg and Westerbork (the shortest baseline is relevant here because the cross-fringe pattern is dominated by the short baselines). This is consistent with the scatter evident in the Gaussian-fit positions on Figure 7 (mean = 70 mas, with standard deviation = 72 mas). It is reasonable to expect an even larger scatter on the peak positions because this combines the uncertainties on the short baselines, as well as on the long baselines. Additionally, the peak positions will be highly influenced by the phase noise on long baselines, which in general is larger than on shorter baselines. We indeed observe a larger mean and scatter on the peak positions than on the Gaussian-fit positions (Figure 7; peaks mean = 164 mas, with standard deviation = 223 mas). Note that we excluded three bursts (B12, B13, and B18) from the Gaussian fits due to the lack of a cross pattern on the dirty maps, which we did not exclude from the peak positions in computing these statistics. By removing the peak positions of those same bursts, we still find a larger mean and scatter compared with the Gaussian fits (peaks mean = 120 mas with standard deviation = 166 mas).

Therefore, due to the lower scatter in the Gaussian-fit positions in Figure 7 compared with the peak positions, we conclude that the safer approach to determine individual burst positions, with an array of <20 baselines, is by using the Gaussian-fit method. In this work, we are assuming that ionospheric turbulence is not varying drastically between observing epochs, or at least that our calibration is correcting for this sufficiently accurately—a fair assumption due to our relatively high observing frequency (>1 GHz). Here we have provided an empirical investigation of astrometric uncertainties using one source at two epochs. This does not allow us to consider a wide range of observing conditions, so future such studies on other sources will be useful in our understanding of the limitations of VLBI FRB localizations.

4.2. The Local Environment of FRB 20201124A

The host galaxy of FRB 20201124A, SDSS J050803.48 +260338.0, hereafter J0508+2603 (Day et al. 2021), is a massive, star-forming galaxy (Fong et al. 2021; Ravi et al. 2021) at a redshift of $z = 0.098$ (Kilpatrick et al. 2021). The VLA (D-configuration; Ricci et al. 2021) detected unresolved compact persistent emission at 3 GHz and 9 GHz, in addition to the uGMRT (Wharton et al. 2021b) detection of unresolved persistent emission at 600 MHz. Follow-up with 22-GHz VLA observations in C configuration allowed for the emission to be resolved (Piro et al. 2021). The lack of compact emission in our EVN 1.4-GHz observations (Figure 2) supports the conclusion that the radio emission seen with lower-resolution instruments is from star formation (Fong et al. 2021; Piro et al. 2021; Ravi et al. 2021).

The milliarcsecond precision of our EVN localization allows us to explore where the FRB location is relative to the radio star formation emission (Piro et al. 2021) and the center of the host galaxy (Fong et al. 2021). We find that FRB 20201124A is 710 ± 30 mas (projected distance: $\sim$1.3 kpc, assuming an angular size distance of 375.9 Mpc; Kilpatrick et al. 2021), from the optical center of the host galaxy, statistically inconsistent with originating from the galaxy center, similar to the discussion in Fong et al. (2021). The uncertainties on this offset arise as the quadrature sum of the radio position uncertainty (4.5 mas), the optical position uncertainty in Pan-STARRS (13 mas; Fong et al. 2021), and the astrometric tie uncertainty between Pan-STARRS and Gaia (22 mas; Magnier et al. 2020). We note that the Gaia reference frame and the ICRF agree on the few-milliarcsecond level (Mignard et al. 2016), therefore the uncertainties on the optical position and frame tying Pan-STARRS to Gaia dominate the error budget. FRB 20201124A is 175 ± 180 mas from the peak of the radio star formation emission, where the uncertainty is dominated by the positional accuracy of the peak of the extended 22-GHz emission (Piro et al. 2021).

Future observations in optical and infrared, using high-resolution instruments such as the Hubble Space Telescope, will allow for a measurement of the proximity of FRB 20201124A with star-forming knots in the host galaxy. This can be compared with the measured 250 pc and 260 pc offset from the peak of a nearby star-forming region in the case of FRB 20180916B (Tendulkar et al. 2021) and FRB 20121102A (Bassa et al. 2017; Kokubo et al. 2017), respectively. Additionally, these observations will allow for the exploration of the role of star formation on the period of high activity (Lanman et al. 2021), the production of extremely bright bursts (Kirsten et al. 2021; Herrmann 2021), as well as the presence of significant circular polarization and polarization angle swings in some bursts from FRB 20201124A (Hilmarsson et al. 2021a; Kumar et al. 2021).

We would like to thank the directors and staff at the various participating stations for allowing us to use their facilities and running the observations. The EVN is a joint facility of independent European, African, Asian, and North American radio astronomy institutes. Scientific results from data presented in this publication are derived from the following EVN project code: EK048. We used the 100 m telescope of the MPIfR (Max-Planck-Institut für Radioastronomie) at Effelsberg. This work was also based on simultaneous EVN and PSRIX data-recording observations with the 100 m Effelsberg telescope, and simultaneous EVN and DFB recordings with the Sardinia 64 m telescope. We thank the local staff for this arrangement. The Sardinia Radio Telescope is funded by the Department of Universities and Research (MIUR), the Italian Space Agency (ASI), and the Autonomous Region of Sardinia (RAS) and is operated as a National Facility by the National Institute for Astrophysics (INAF). This work is based in part on observations carried out using the 32 m Badary, Svetloe, and Zelenchukskaya radio telescopes operated by the Scientific Equipment Sharing Center of the Quasar VLBI Network (Russia). This work is based in part on observations carried out using the 32 m radio telescope operated by the Institute of Astronomy of the Nicolaus Copernicus University in Toruń

(Poland) and supported by a Polish Ministry of Science and Higher Education SpUBgrant.

This project has received funding from the European Union's Horizon 2020 research and innovation program under grant agreements nos. 730562 (RadioNet) and 101004719 (OPTICON-RadioNet Pilot). Research by the AstroFlash group at the University of Amsterdam, ASTRON, and JIVE is supported in part by an NWO Vici grant (PI Hessels; VI. C.192.045). B.M. acknowledges support from the Spanish Ministerio de Economía y Competitividad (MINECO) under grant AYA2016-76012-C3-1-P and from the Spanish Ministerio de Ciencia e Innovación under grants PID2019-105510GB-C31 and CEX2019-000918-M of ICCUB (Unidad de Excelencia "María de Maeztu" 2020–2023). J.P.Y. is supported by the National Program on Key Research and Development Project (2017YFA0402602). N.W. acknowledges support from the National Natural Science Foundation of China (grants 12041304 and 11873080).

ORCID iDs

K. Nimmo https://orcid.org/0000-0003-0510-0740
D. M. Hewitt https://orcid.org/0000-0002-5794-2360
J. W. T. Hessels https://orcid.org/0000-0003-2317-1446
F. Kirsten https://orcid.org/0000-0001-6664-8668
B. Marcote https://orcid.org/0000-0001-9814-2354
U. Bach https://orcid.org/0000-0002-7722-8412
R. Blaauw https://orcid.org/0000-0003-1771-1012
M. Burgay https://orcid.org/0000-0002-8265-4344
A. Corongiu https://orcid.org/0000-0002-5924-3141
R. Feiler https://orcid.org/0000-0002-9812-2078
M. P. Gawroński https://orcid.org/0000-0003-4056-4903
M. Giroletti https://orcid.org/0000-0002-8657-8852
R. Karuppusamy https://orcid.org/0000-0002-5307-2919
A. Keimpema https://orcid.org/0000-0002-5575-2774
M. A. Kharinov https://orcid.org/0000-0002-0321-8588
M. Lindqvist https://orcid.org/0000-0002-3669-0715
G. Maccaferri https://orcid.org/0000-0002-1482-708X
A. Melnikov https://orcid.org/0000-0002-8466-7026
A. Mikhailov https://orcid.org/0000-0002-3355-2261
O. S. Ould-Boukattine https://orcid.org/0000-0001-9381-8466
Z. Paragi https://orcid.org/0000-0002-5195-335X
M. Pilia https://orcid.org/0000-0001-7397-8091
A. Possenti https://orcid.org/0000-0001-5902-3731
M. P. Snelders https://orcid.org/0000-0001-6170-2282
G. Surcis https://orcid.org/0000-0003-2775-442X
M. Trudu https://orcid.org/0000-0002-1530-0474
T. Venturi https://orcid.org/0000-0002-8476-6307
W. Vlemmings https://orcid.org/0000-0002-2700-9916
N. Wang https://orcid.org/0000-0002-9786-8548
J. Yang https://orcid.org/0000-0002-2322-5232

References

Agarwal, D., Aggarwal, K., Burke-Spolaor, S., Lorimer, D. R., & Garver-Daniels, N. 2020, MNRAS, 497, 1661
Bannister, K. W., Deller, A. T., Phillips, C., et al. 2019, Sci, 365, 565
Bassa, C. G., Tendulkar, S. P., Adams, E. A. K., et al. 2017, ApJL, 843, L8
Bhandari, S., Heintz, K. E., Aggarwal, K., et al. 2021, AJ, 163, 69
Bhardwaj, M., Gaensler, B. M., Kaspi, V. M., et al. 2021, ApJL, 910, L18
Chatterjee, S., Law, C. J., Wharton, R. S., et al. 2017, Natur, 541, 58
Chime/Frb Collaboration 2021, ATel, 14497, 1
CHIME/FRB Collaboration, Amiri, M., Bandura, K., et al. 2018, ApJ, 863, 48
Cordes, J. M., & Chatterjee, S. 2019, ARA&A, 57, 417
Cordes, J. M., & McLaughlin, M. A. 2003, ApJ, 596, 1142
Crane, P. C., & Napier, P. J. 1989, in ASP Conf. Ser. 6, Synthesis Imaging in Radio Astronomy, ed. R. A. Perley, F. R. Schwab, & A. H. Bridle (San Francisco, CA: ASP), 139
Day, C. K., Bhandari, S., Deller, A. T., Shannon, R. M., & Moss, V. A. 2021, ATel, 14515, 1
Fong, W.-f., Dong, Y., Leja, J., et al. 2021, ApJL, 919, L23
Gajjar, V., Siemion, A. P. V., Price, D. C., et al. 2018, ApJ, 863, 2
Gajjar, V., Perez, K. I., Siemion, A. P. V., et al. 2021, AJ, 162, 33
Gourdji, K., Michilli, D., Spitler, L. G., et al. 2019, ApJL, 877, L19
Greisen, E. W. 2003, in Information Handling in Astronomy—Historical Vistas, Astrophysics and Space Science Library, 285, ed. A. Heck (Dordrecht: Kluwer), 109
Heintz, K. E., Prochaska, J. X., Simha, S., et al. 2020, ApJ, 903, 152
Herrmann, W. 2021, ATel, 14556, 1
Hewitt, D. M., Snelders, M. P., Hessels, J. W. T., et al. 2021, arXiv:2111.11282
Hilmarsson, G. H., Spitler, L. G., Main, R. A., & Li, D. Z. 2021a, MNRAS, 508, 5354
Hilmarsson, G. H., Michilli, D., Spitler, L. G., et al. 2021b, ApJL, 908, L10
Hotan, A. W., van Straten, W., & Manchester, R. N. 2004, PASA, 21, 302
Keimpema, A., Kettenis, M. M., Pogrebenko, S. V., et al. 2015, ExA, 39, 259
Kilpatrick, C. D., Fong, W., Prochaska, J. X., et al. 2021, ATel, 14516, 1
Kirsten, F., Vlemmings, W., Campbell, R. M., Kramer, M., & Chatterjee, S. 2015, A&A, 577, A111
Kirsten, F., Marcote, B., Nimmo, K., et al. 2022, Natur, 602, 585
Kirsten, F., Ould-Boukattine, O. S., Nimmo, K., et al. 2021, ATel, 14605, 1
Kokubo, M., Mitsuda, K., Sugai, H., et al. 2017, ApJ, 844, 95
Kumar, P., Shannon, R. M., Lower, M. E., et al. 2021, arXiv:2109.11535
Lanman, A. E., Andersen, B. C., Chawla, P., et al. 2021, arXiv:2109.09254
Law, C., Tendulkar, S., Clarke, T., Aggarwal, K., & Bethapudy, S. 2021, ATel, 14526, 1
Lazarus, P., Karuppusamy, R., Graikou, E., et al. 2016, MNRAS, 458, 868
Li, D., Wang, P., Zhu, W. W., et al. 2021, Natur, 598, 267
Magnier, E. A., Schlafly, E. F., Finkbeiner, D. P., et al. 2020, ApJS, 251, 6
Main, R. A., Hilmarsson, G. H., Marthi, V. R., et al. 2022, MNRAS, 509, 3172
Mannings, A. G., Fong, W.-f., Simha, S., et al. 2021, ApJ, 917, 75
Marcote, B., Paragi, Z., Hessels, J. W. T., et al. 2017, ApJL, 834, L8
Marcote, B., Nimmo, K., Hessels, J. W. T., et al. 2020, Natur, 577, 190
Marcote, B., Kirsten, F., Hessels, J. W. T., et al. 2021, ATel, 14603, 1
Martí-Vidal, I., Guirado, J. C., Jiménez-Monferrer, S., & Marcaide, J. M. 2010a, A&A, 517, A70
Martí-Vidal, I., Ros, E., Pérez-Torres, M. A., et al. 2010b, A&A, 515, A53
Michilli, D., Seymour, A., Hessels, J. W. T., et al. 2018a, Natur, 553, 182
Michilli, D., Hessels, J. W. T., Lyon, R. J., et al. 2018b, MNRAS, 480, 3457
Mignard, F., Klioner, S., Lindegren, L., et al. 2016, A&A, 595, A5
Nimmo, K., Hessels, J. W. T., Kirsten, F., et al. 2022, NatAs, https://www.nature.com/articles/s41550-021-01569-9
Noll, C. E. 2010, AdSpR, 45, 1421
Petroff, E., Hessels, J. W. T., & Lorimer, D. R. 2019, A&ARv, 27, 4
Petroff, E., Hessels, J. W. T., & Lorimer, D. R. 2021, arXiv:2107.10113
Piro, L., Bruni, G., Troja, E., et al. 2021, A&A, 656, L15
Plavin, A. V., Kovalev, Y. Y., Pushkarev, A. B., & Lobanov, A. P. 2019, MNRAS, 485, 1822
Pleunis, Z., Good, D. C., Kaspi, V. M., et al. 2021a, ApJ, 923, 1
Pleunis, Z., Michilli, D., Bassa, C. G., et al. 2021b, ApJL, 911, L3
Prandoni, I., Murgia, M., Tarchi, A., et al. 2017, A&A, 608, A40
Ransom, S. M. 2001, PhD thesis, Harvard University
Ravi, V., Catha, M., D'Addario, L., et al. 2019, Natur, 572, 352
Ravi, V., Law, C. J., Li, D., et al. 2021, arXiv:2106.09710
Reich, P., & Reich, W. 1988, A&A, 196, 211
Remazeilles, M., Dickinson, C., Banday, A. J., Bigot-Sazy, M. A., & Ghosh, T. 2015, MNRAS, 451, 4311
Ricci, R., Piro, L., Panessa, F., et al. 2021, ATel, 14549, 1
Shepherd, M. C., Pearson, T. J., & Taylor, G. B. 1994, BAAS, 26, 987
Tendulkar, S. P., Bassa, C. G., Cordes, J. M., et al. 2017, ApJL, 834, L7
Tendulkar, S. P., Gil de Paz, A., Kirichenko, A. Y., et al. 2021, ApJL, 908, L12
van Straten, W., & Bailes, M. 2011, PASA, 28, 1
Wharton, R., Bethapudi, S., Marthi, V., et al. 2021a, ATel, 14538, 1
Wharton, R., Bethapudi, S., Gautam, T., et al. 2021b, ATel, 14529, 1
Whitney, A. 2004, in Proc. of the European VLBI Network on New Developments in VLBI Science and Technology, 7, ed. R. Bachiller et al. (Madrid: Observatorio Astronomico Nacional of Spain), 251
Whitney, A., Kettenis, M., Phillips, C., & Sekido, M. 2010, in International VLBI Service for Geodesy and Astronomy, Proc. from the 2010 General Meeting, VLBI2010: From Vision to Reality, 6, ed. D. Behrend et al. (Scotts Valley, CA: Create Space), 192